Block modeling of crustal deformation in Tierra del Fuego from GNSS velocities

CrossMark

L. Mendoza [a,b,*], A. Richter [a,b,c], M. Fritsche [c,d], J.L. Hormaechea [a,b], R. Perdomo [a,b], R. Dietrich [c]

[a] Departamento de Astrometría, Facultad de Ciencias Astronómicas y Geofísicas (FCAG), Universidad Nacional de La Plata (UNLP), La Plata, Argentina
[b] Consejo Nacional de Investigaciones Científicas y Técnicas (CONICET), Argentina
[c] Institut für Planetare Geodäsie (IPG), Technische Universität Dresden (TUD), Dresden, Germany
[d] Now at GeoForschungsZentrum (GFZ), Potsdam, Germany

A B S T R A C T

The Tierra del Fuego (TDF) main island is divided by a major transform boundary between the South America and Scotia tectonic plates. Using a block model, we infer slip rates, locking depths and inclinations of active faults in TDF from inversion of site velocities derived from Global Navigation Satellite System observations. We use interseismic velocities from 48 sites, obtained from field measurements spanning 20 years. Euler vectors consistent with a simple seismic cycle are estimated for each block. In addition, we introduce far-field information into the modeling by applying constraints on Euler vectors of major tectonic plates. The difference between model and observed surface deformation near the Magallanes Fagnano Fault System (MFS) is reduced by considering finite dip in the forward model. For this tectonic boundary global plate circuits models predict relative movements between 7 and 9 mm yr^{-1}, while our regional model indicates that a strike-slip rate of 5.9 $\pm$ 0.2 mm yr^{-1} is accommodated across the MFS. Our results indicate faults dipping $66^{+6}_{-4}°$ southward, locked to a depth of 11^{+5}_{-5} km, which are consistent with geological models for the MFS. However, normal slip also dominates the fault perpendicular motion throughout the eastern MFS, with a maximum rate along the Fagnano Lake.

© 2015 Elsevier B.V. All rights reserved.

1. Introduction

The Tierra del Fuego (TDF) main island, southernmost South America, is bisected by the active transform boundary between the South America (SAM) and Scotia (SCO) tectonic plates (Pelayo and Wiens, 1989). In the TDF region, the plate boundary is represented by the Magallanes Fagnano Fault System (MFS, Lodolo et al., 2003). The MFS extends from the Atlantic offshore to the western arm of the Strait of Magellan and splits the TDF island into two continental blocks. The E–W strike and relative movement of the MFS through the southern part of the island produce robust topography and geomorphology, expressed as a series of lineaments and depressions (Irigoyen River valley, Turbio River valley, Fagnano Lake) (e.g., Lodolo et al., 2003; Menichetti et al., 2008). The main trace of the MFS probably provides the trans-extensional forces that produce the 105 km-long Fagnano Lake. This trace exits the lake toward the northwest.

In 1993, geodetic GPS observations were commenced in the Argentine part of the TDF region with the aim to determine the recent relative crustal movements along the MFS. These observations allowed the first detection of the relative horizontal displacement between the northern and southern part of the island (Del Cogliano et al., 2000). Based on an independent set of GPS data, of limited spatial resolution and observation time-span, a first attempt was made to characterize the tectonic deformation along the MFS by a simple kinematic model (Smalley et al., 2003). However, this model assumed an infinitely extended, vertical fault plane, neglecting the actual geometry of the faults' surface traces, and was not able to reliably resolve a locking depth nor a fault inclination. A substantial densification of our regional GPS network lead to a detailed quantitative description of the horizontal surface deformation by means of a strain analysis (Mendoza et al., 2011). These results were based on episodic GPS-only observations carried out until 2008. However, no model for the deformation was proposed.

In this paper we use high quality GNSS data that have enough spatial coverage to begin probing the deep structure of fault slip in this major continental transform tectonic system. Our analysis derived from these geodetic observations aims to complement the knowledge on the present-day dynamics of the MFS. Understanding the many subtle aspects of physical structure of such systems (e.g., Moody and Hill, 1956; Sylvester, 1988) may aid in illuminating the physics controlling aseismic and seismic partitioning of deformation. More generally, this is also a problem of great societal importance since the earthquake potential of this strike-slip system in TDF could endanger population centers and fundamental infrastructure (e.g. natural gas pipelines).

* Corresponding author at: Facultad de Ciencias Astronómicas y Geofísicas, Paseo del Bosque s/n, B1900FWA, Buenos Aires, Argentina.
  E-mail address: lmendoza@fcaglp.unlp.edu.ar (L. Mendoza).

2. Data and methods

2.1. Geodetic observations

We collected campaign-type GPS observations in the TDF area since late 1993. Moreover, the number of observed sites has been steadily growing, and during 2010 to 2013 many semi-permanent GNSS stations were installed, recording continuously for several months. In addition, selected tracking stations from the International GNSS Service (IGS) were included in the analysis, some of which have GPS + GLONASS capabilities since 2006. In total, the regional measurements set spans 20 years, and has sufficient precision and distribution to reliably infer deformation at near-fault spatial scale. This densification also allows for the estimation of a second invariant of the strain rate tensor, possibly with improved signal to noise ratio (e.g., Kreemer et al., 2014).

2.2. GNSS data analysis

The observations were processed with the *Bernese Software* version 5.1 (Dach et al., 2007), and models recommended by the International Earth Rotation Service (IERS) were used (Petit and Luzum, 2010). In addition, ocean tidal loading corrections, according to Savcenko and Bosch (2012), and absolute phase-center corrections for satellites and receivers, as issued by the IGS (file *IGS08.atx*), were applied. The tropospheric delay was modeled with the Global Mapping Function (GMF, Boehm et al., 2006), including 2-hourly zenith delay estimates. First order ionospheric delays were eliminated by means of the ionosphere-free linear combination, and higher-order terms were modeled according to Fritsche et al. (2005). The IGS08 reference frame (Rebischung et al., 2012) was introduced by means of constraints on coordinates of selected IGS tracking sites. To assure a homogeneous set of GPS + GLONASS precise orbits and clocks, and consistent Earth Orientation Parameters (EOP), the reprocessed products computed by Fritsche et al. (2014) were used. These reprocessing products extend from late 1993 to early 2013 and were supplemented with operational IGS products covering the time period from 2013 to early 2014.

Too optimistic formal uncertainties for the site velocities are typically obtained from the GNSS data analysis (e.g., Mao et al., 1999). This is due to the fact that a simplified correlation dependency is assumed (non differenced observations are considered to be uncorrelated) and also due to the huge number of observations adjusted (in our case 3.4×10^8 double differenced ionosphere-free linear combinations were simultaneously inverted). Therefore, and in order to obtain realistic uncertainties for the velocity estimates, the position time series were analyzed. For every site, trends and trends' uncertainties for the north and east components, together with white and flicker noise parameters, were estimated by means of the software tool *CATS* (Williams, 2003). On average, the realistic uncertainties were 20 times larger than the formal uncertainties obtained from the least squares adjustment of GNSS observations. Therefore, a scaling factor of $400 = 20^2$ was applied to the whole variance–covariance matrix of the velocity estimates as obtained from the GNSS analysis. In our modeling the velocities resulting from the multi-year GNSS cumulative solution, together with their rescaled uncertainties, were used as input observations.

2.3. Strain analysis

In order to quantify the surface deformation associated to the MFS main deformation zone, a locally uniform strain rate field was computed by inverting the observed velocities (Shen et al., 2007). The three components of the strain rate tensor ($\dot{\epsilon}_{ee}, \dot{\epsilon}_{nn}, \dot{\epsilon}_{en}$), together with a rigid rotation rate, were estimated for each point of a regular grid, every 5 km, near the plate boundary.

This method does not require an optimal Delaunay triangulation nor assume uniform deformation within polygons. The inversions were carried out by least squares adjustments, where the observed velocities were reweighted by a factor Ae^{-d^2/σ^2}. Here, A weights the contribution of each site according to the area of its corresponding cell in a Voronoi tessellation of the sites' locations, whereas d is the distance between the site and the point being evaluated and σ is a smoothing factor, in this case equal to 30 km. Note that only the area of each Voronoi cell was employed in the adjustments. The strain rate field was modeled as a smooth and continuous function, regardless of the cell's boundaries. Finally, the second invariant of the strain rate, defined as $\sqrt{\dot{\epsilon}_{ee}^2 + \dot{\epsilon}_{nn}^2 + 2\dot{\epsilon}_{en}^2}$ (Kreemer et al., 2003), was computed for every point of the grid.

2.4. Block modeling

In this work, the methodology described by Meade and Hager (2005) was applied. The model relates block motions and fault slip rates to observed interseismic deformation, and makes use of the analytic solutions given by Okada (1985) for the surface deformation due to an arbitrarily inclined and finite dislocation in a homogeneous elastic half-space.

Given a block partition (bounded by faults), fault segments $\left(\vec{x}_F\right)$ and site locations $\left(\vec{x}_S\right)$, the interseismic velocity is interpreted as the difference between the block velocity and the coseismic slip deficit (CSD) velocity

$$\vec{v}_I = \vec{v}_B\left(\vec{x}_S\right) - \vec{v}_{CSD}\left(\vec{x}_S, \vec{x}_F\right). \tag{1}$$

Both the block and the CSD velocities are expressed as linear transformations of Euler poles and rotation rates

$$\vec{v}_B = \mathbf{R}_E\mathbf{R}_B\vec{\Omega} = \mathbf{R}_1\vec{\Omega} \tag{2}$$

$$\vec{v}_{CSD} = \mathbf{R}_M\mathbf{R}_O\underbrace{\mathbf{R}_F\mathbf{R}_{\Delta\vec{v}}\vec{\Omega}}_{\vec{s}} = \mathbf{R}_2\vec{\Omega} \tag{3}$$

where $\mathbf{R}_B\vec{\Omega} = \vec{\Omega} \times \vec{x}_S$ account for the relative block rotation, $\mathbf{R}_E$ transforms from a geocentric $\{x, y, z\}$ into a local $\{e, n\}$ system, $\mathbf{R}_{\Delta\vec{v}}$ gives the fault-parallel and fault-normal relative velocity vector $\Delta\vec{v} = (v_\parallel, v_\perp)$, $\mathbf{R}_F$ projects this velocity vector into Okada's coordinate system, $\mathbf{R}_O$ contains the partial derivatives of Okada's elastic Green's functions with respect to each component of the slip rate vector $\vec{s}$ and $\mathbf{R}_M$ computes the inverse projection from Oblique Mercator (oriented along each fault segment) into a local $\{e, n\}$ system. Finally, if a priori information from geodetic or geophysical studies is available, either as absolute $\left(\vec{\Omega}\right)$ or relative $\left(\vec{\Omega}_{ij}\right)$ Euler poles and rotation rates, the forward model can be written as

$$\begin{pmatrix} \vec{v}_I \\ \vec{\Omega} \\ \vec{\Omega}_{ij} \end{pmatrix} = \begin{pmatrix} \mathbf{R}_1 - \mathbf{R}_2 \\ \mathbf{I} \\ \mathbf{I}_{ij} \end{pmatrix} \vec{\Omega} \tag{4}$$

where $\mathbf{I}$ is the identity matrix and $\mathbf{I}_{ij}$ accounts for the relative rotation of block i with respect to block j. Rewriting this model as $\vec{d} = \mathbf{R}\vec{\Omega}$, the Euler pole and rotation rate of each block can be estimated by linear least squares

$$\widehat{\vec{\Omega}} = \left(\mathbf{R}^T\mathbf{W}\mathbf{R}\right)^{-1}\mathbf{R}^T\mathbf{W}\vec{d} \tag{5}$$

where $\mathbf{W}$ contains weights for the observations and appropriate constraints for the pseudo observations (i.e., a priori Euler poles and rotation rates). In turn, the slip vector accommodated by each fault segment can

be computed from Eq. (3). We refer to Meade and Hager (2005) for further detail about this method.

In our work, the geometry of each fault segment was characterized by its trace on the surface, a dip angle (δ) and a locking depth (D). Each fault segment was allowed to accommodate either strike- and dip-slip (for $\delta \neq 90°$, i.e., inclined fault) or strike- and tensile-slip (for $\delta = 90°$, i.e., vertical fault) (Fig. 1). Okada's expressions were implemented by means of modified routines from the software package *dModels* (Battaglia et al., 2013a,b).

Given a block partition, a fixed set of fault segment traces, and assuming common inclination and locking depth for all fault segments, the solution space for the non-linear parameters δ and D was studied. For δ ranging from quasi-horizontal to vertical, and for D ranging from the surface to a maximum depth, Eq. (5) was solved for $\vec{\Omega}$ at every node of a regular grid (with $\Delta\delta = 5°$ and $\Delta D = 1$ km). The δ and D nodes resulting in the lowest sum of weighted residuals (χ^2), for both the inclined and vertical fault cases, were selected. To obtain final estimates, these values were used as a starting point in a gradient descent algorithm, on the real domain, with cost function χ^2. Finally, consistent Euler poles, rotation rates, and slip rate vectors were estimated for each optimum pair δ and D.

To assess the uncertainty of the non-linear parameters the bootstrap method was employed (Árnadóttir and Segall, 1994). Using a Monte Carlo algorithm, 10^3 samples of site velocities (with replace) were synthesized and the corresponding non-linear parameters were optimized. For each parameter, the complete sequence of solutions was sorted and the two-sided bootstrap percentile interval was obtained (at 95% confidence level).

2.5. Model geometry and constraints

The TDF area was modeled as two blocks, at north and south of the MFS (SAM and SCO blocks, respectively) (Fig. 2b). These blocks were bounded by three fault segments (Segment 1 along Irigoyen River, Segment 2 along central eastern Fagnano Lake and Segment 3 along western Fagnano Lake and Azopardo River). These segments are simplifications of fault traces from surface geology (Tassone et al., 2005) and were not included as unknowns in the adjustment to minimize the high correlations typically observed between fault geometry and kinematic parameters (Freymueller et al., 1999). A total of 48 sites are located in the area, 31 on the SAM block and 17 on the SCO block (Table 1).

The absolute Euler pole and rotation rate for the SAM plate referring to a no-net-rotation frame (Drewes, 2009, model APKIM2005IGN) were added as pseudo observations ($\varphi = -14.6° \pm 0.9°$, $\lambda = -122° \pm 1.5°$, $\omega = +0.123 \pm 0.002$ deg Myr^{-1}). Similarly, the relative pole and rotation rate for the SCO plate with respect to fixed SAM (Thomas et al., 2003, model TLP2003) were introduced ($\varphi = +19.074° \pm 39.9°$, $\lambda = -56.906° \pm 5.8°$, $\omega = +0.067 \pm 0.01$ deg Myr^{-1}). Both

Euler poles and rates were loosely constrained at a 3-σ level. In addition, the local observations were weighted according to the realistic variances computed from the position time series (Fig. 3).

3. Results

3.1. Observed interseismic deformation

Our velocity estimates are derived from the geodetic observations with respect to the global terrestrial reference frame IGS08 and are listed together with their corresponding uncertainties in Table 1. The analysis of the residual position time series, besides providing the common scale factor for the uncertainties, revealed no indication of non-linear movement on any site. A systematic difference in the magnitude and direction of the displacements, at each side of the fault segments, could be observed (Fig. 2c). This is consistent with the left-lateral movement accommodated across this tectonic boundary (Bird, 2003). Moreover, the strain analysis revealed the main deformation zone associated to the MFS, which extends approximately 40 km to the north and south of the system's main trace, and includes an area of maximum extensional rates along Fagnano Lake's basin (Fig. 2d).

3.2. Block modeling

The inversion of the velocity estimates alone, without any additional constraints, resulted in poorly resolved Euler poles and rates, for both the vertical and inclined fault cases (Models 1 and 2, respectively). For Model 1 this also propagated to the non-linear parameter (any depth between 10 and 20 km produced practically the same χ^2, Fig. 4a). In comparison, the non-linear parameters for Model 2 were better resolved (Table 3). In this case a significant inclination was found, clearly not near-vertical, with fault segments dipping to the south (Fig. 4c), under SCO plate. While the fit of both models with the observations was comparable, the vertical model (Model 1) requires a distinctive location for the Euler pole of the SAM block (Table 2), far away from any a priori estimate for the SAM plate (e.g., Drewes, 2009; Bird, 2003). In turn, this different location of estimated Euler poles produced alternatively closing (Model 1) or opening (Model 2) movement across the eastern fault segment (Table 3). Also, Model 1 requires 15% faster strike-slip rates, along all fault segments, to reproduce the observed deformation.

The effect of the additional geophysical constraints was twofold. As expected, the estimated absolute (and relative) Euler poles and rates were closer to their a priori values, for both the vertical and inclined fault cases (Models 1c and 2c, respectively). Also, compared to the unconstrained Models 1 and 2, the only slight increase in χ^2 for the constrained models indicates that the a priori values were not overconstrained (Table 2). On the other hand, Euler poles and rates were much better resolved, in comparison to the unconstrained models (i.e., uncertainties one order of magnitude smaller). In particular, for Model 1c a much better constrained locking depth was found (Fig. 4b). In contrast, Model 2c resulted in optimum fault inclination and locking depth similar to the values found for Model 2, and also similarly resolved (Table 3). In addition, predicted closing and opening movement, across all fault segments, were consistent between both Model 1c and 2c (implying tensile- or dip-slip rates, respectively, Table 3). Nevertheless, an *F*-ratio test shows that the decrease in χ^2, between constrained vertical and inclined models, is significant at a 95% confidence level. Therefore, we prefer the constrained model with inclined fault segments (Model 2c).

4. Discussion

One of the main goals of this work is to quantitatively characterize the continuum strain rate field of the main portion of the interplate shear concentrated in the MFS using inversions of observed interseismic
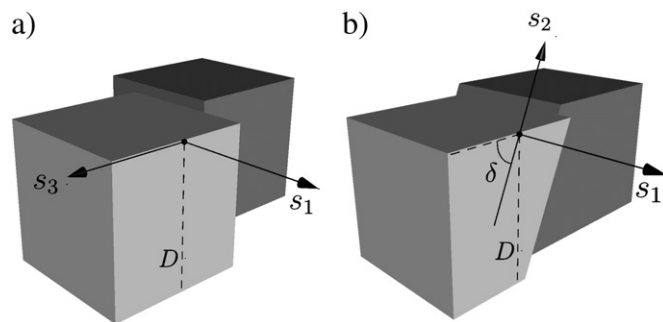

Fig. 1. a) Vertical dislocations are characterized by a locking depth (D) and strike- and tensile-slip rates (s_1 and s_3, respectively); b) inclined dislocations are characterized by a dip angle (δ), a locking depth (D) and strike- and dip-slip rates (s_1 and s_2, respectively).
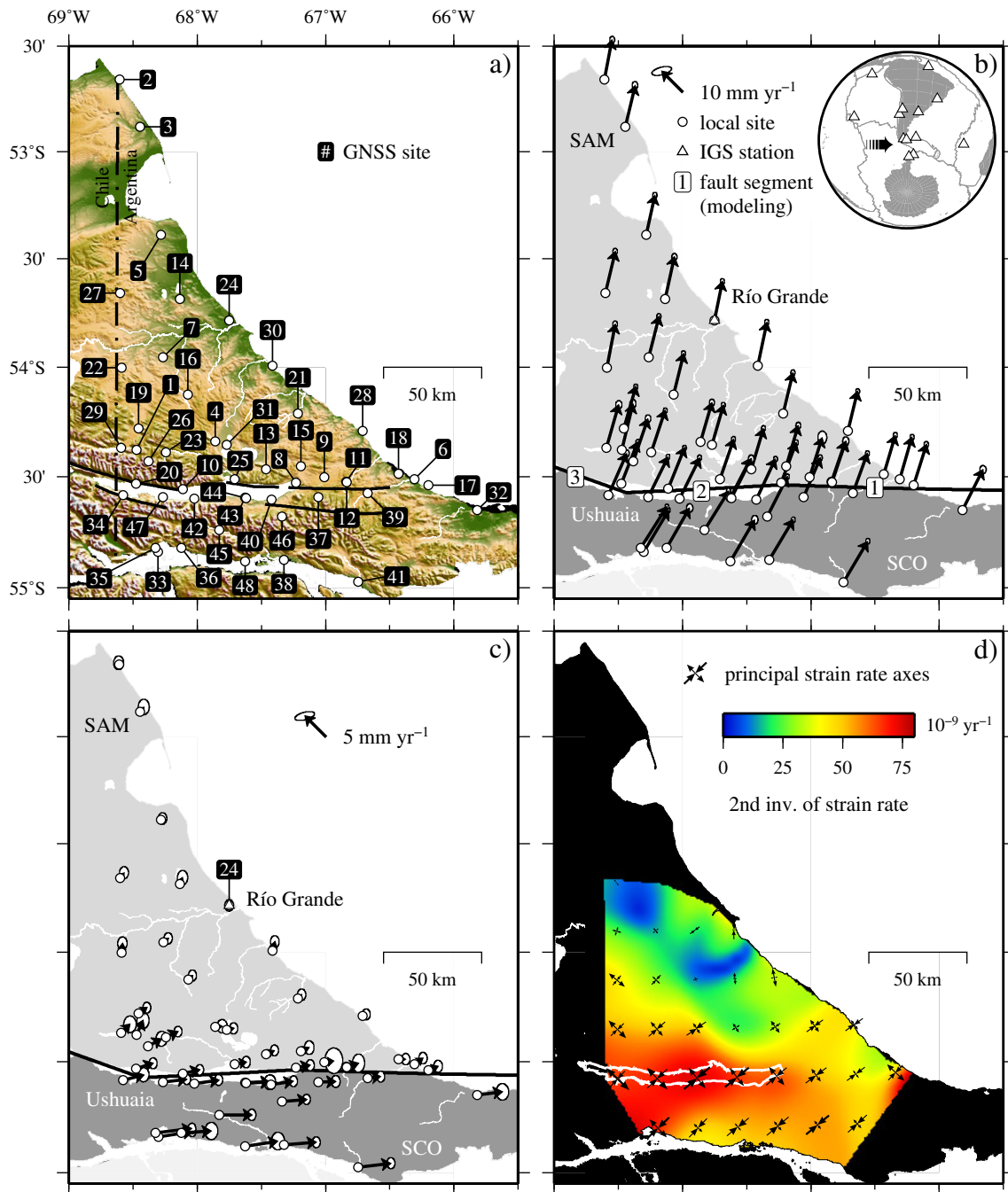
Fig. 2. a) Location of the regional GNSS sites listed in Table 1 and main transcurrent faults associated to the MFS (Tassone et al., 2005; Esteban et al., 2014). Regional SRTM topography as background (Rodrguez et al., 2005). b) Observed interseismic velocities for the regional GNSS sites, referred to the terrestrial reference frame IGS08 (Rebischung et al., 2012). The geometry for the block model is shown: three fault segments (1, 2, and 3) and two blocks (SCO and SAM). Globe: reference IGS tracking stations and mayor tectonic boundaries (Bird, 2003). The black arrow indicates the working area in southernmost South America. c) The same observed velocities, but referred to the IGS tracking station RIOG (regional site 24); in this case, the scale for the velocities is two times larger than in b). d) Near-fault surface deformation obtained by inverting the observed interseismic velocities (color coded: magnitude of the second invariant of the strain rate). The principal strain rate axes and the shoreline of the Fagnano Lake, in white, are also shown.

velocities. In addition, we are able to constrain some geometrical and kinematic parameters of the fault system that constitutes the main source for the observed deformation. For this purpose, the block modeling provides not only a solution consistent over both geological and geodetic timescales but also simplifies the introduction of far-field information by means of geophysical constraints (Meade and Hager, 2005). While the fault segment traces were adopted from geological studies, we were able to estimate characteristic locking depths, fault inclinations

and slip rates along the fault system. Although it is a simplification, our preferred model closely matches the observed deformation (Fig. 5).

The ~ 6 mm yr^{-1} of left-lateral movement accommodated across the MFS, according to our results, is consistent with the estimation given by Thomas et al. (2003) for this segment of the plate boundary (7.0 ± 3.5 mm yr^{-1}). Also, a rate of ~ 7 mm yr^{-1} is predicted by the geodetically constrained model GSRM-NNR-2 (Kreemer et al., 2006). However, it is important to note that this model incorporates the results

Table 1
Observed interseismic velocities for the regional GNSS sites.

Site #	Latitude deg	Longitude deg	Year of 1st occup.	Year of last occup.	# of 24 h sessions[a]	Installation type[b]	Observation type[c]	Block (modeling)	v_n mm yr^{-1}	v_e mm yr^{-1}
1	− 54.378	− 68.472	2010	2014	14	D	G + R	SAM	15.7 ± 0.5	3.8 ± 0.3
2	− 52.659	− 68.606	2008	2014	12	T	G	SAM	13.5 ± 0.4	2.6 ± 0.3
3	− 52.881	− 68.447	1993	2011	11	T/A	G	SAM	14.0 ± 0.4	3.4 ± 0.3
4	− 54.341	− 67.859	2010	2013	218	D	G + R	SAM	13.3 ± 0.4	3.8 ± 0.3
5	− 53.388	− 68.283	2005	2013	78	D	G + R	SAM	13.4 ± 0.3	2.9 ± 0.2
6	− 54.511	− 66.306	2007	2014	27	D	G	SAM	14.3 ± 0.3	4.1 ± 0.2
7	− 53.955	− 68.265	1993	2013	71	T/A	G + R	SAM	13.9 ± 0.3	3.5 ± 0.2
8	− 54.528	− 67.231	1993	2011	57	D	G	SAM	13.7 ± 0.3	5.1 ± 0.2
9	− 54.502	− 67.008	2010	2013	19	D	G	SAM	13.4 ± 0.7	4.3 ± 0.5
10	− 54.556	− 68.113	2003	2014	42	D	G	SAM	13.9 ± 0.3	5.6 ± 0.2
11	− 54.523	− 66.838	2004	2013	34	T/A	G	SAM	13.7 ± 0.3	4.7 ± 0.2
12	− 54.525	− 66.836	2004	2013	7	T/A	G	SAM	13.9 ± 0.5	4.7 ± 0.3
13	− 54.466	− 67.464	2003	2013	38	T/A	G	SAM	13.9 ± 0.3	4.1 ± 0.2
14	− 53.687	− 68.134	1993	2011	17	T	G	SAM	14.4 ± 0.4	3.1 ± 0.3
15	− 54.454	− 67.191	2008	2013	29	D	G	SAM	13.9 ± 0.4	4.1 ± 0.3
16	− 54.126	− 68.071	1993	2013	29	T/A	G	SAM	13.9 ± 0.3	3.4 ± 0.2
17	− 54.540	− 66.201	2007	2014	26	D	G	SAM	13.9 ± 0.3	4.4 ± 0.2
18	− 54.488	− 66.431	2007	2013	92	D	G + R	SAM	13.2 ± 0.3	3.9 ± 0.2
19	− 54.282	− 68.457	2003	2014	34	D	G	SAM	14.3 ± 0.3	4.1 ± 0.2
20	− 54.533	− 68.475	2003	2014	30	D	G	SAM	14.2 ± 0.3	5.6 ± 0.2
21	− 54.213	− 67.216	1993	2011	37	T/A	G	SAM	13.9 ± 0.3	3.3 ± 0.2
22	− 54.003	− 68.590	1993	2013	20	T/A	G	SAM	14.8 ± 0.3	2.9 ± 0.3
23	− 54.390	− 68.242	1993	2014	47	T/A	G	SAM	14.2 ± 0.3	4.7 ± 0.2
24	− 53.785	− 67.751	2000	2014	cont.[d]	D	G + R	SAM	13.2 ± 0.3	2.7 ± 0.2
25	− 54.512	− 67.710	2003	2011	32	D	G	SAM	13.6 ± 0.3	4.7 ± 0.2
26	− 54.430	− 68.381	2010	2014	17	D	G + R	SAM	14.5 ± 0.4	5.0 ± 0.3
27	− 53.658	− 68.602	1993	2013	18	T	G	SAM	14.1 ± 0.4	3.4 ± 0.3
28	− 54.293	− 66.710	1993	2013	39	T/A	G	SAM	13.5 ± 0.3	3.3 ± 0.2
29	− 54.370	− 68.592	2010	2014	20	D	G + R	SAM	14.7 ± 0.5	4.2 ± 0.4
30	− 53.993	− 67.414	1993	2011	26	T/A	G	SAM	14.8 ± 0.3	3.1 ± 0.2
31	− 54.356	− 67.772	1993	2011	32	T/A	G	SAM	13.5 ± 0.3	3.9 ± 0.2
32	− 54.652	− 65.818	2011	2014	12	D	G + R	SCO	13.8 ± 0.5	7.0 ± 0.4
33	− 54.840	− 68.304	2007	2014	cont.[d]	D	G	SCO	14.1 ± 0.4	8.5 ± 0.2
34	− 54.583	− 68.578	2010	2014	16	D	G + R	SCO	14.1 ± 0.4	6.2 ± 0.3
35	− 54.823	− 68.324	1993	2014	43	D	G	SCO	14.0 ± 0.3	8.9 ± 0.2
36	− 54.822	− 68.122	2011	2014	16	D	G + R	SCO	13.6 ± 0.5	7.8 ± 0.4
37	− 54.593	− 67.058	2004	2011	20	D	G	SCO	13.3 ± 0.3	5.7 ± 0.2
38	− 54.876	− 67.324	1997	2013	35	D	G + R	SCO	13.7 ± 0.3	8.2 ± 0.2
39	− 54.575	− 66.672	2005	2013	40	D	G	SCO	13.5 ± 0.3	4.9 ± 0.2
40	− 54.604	− 67.423	2003	2013	35	T/A	G + R	SCO	13.8 ± 0.3	6.5 ± 0.2
41	− 54.975	− 66.745	1993	2013	35	T/A	G	SCO	13.9 ± 0.3	8.2 ± 0.2
42	− 54.599	− 68.024	2003	2012	32	D	G	SCO	13.8 ± 0.3	6.9 ± 0.2
43	− 54.595	− 67.625	2003	2012	38	D	G	SCO	13.4 ± 0.4	6.9 ± 0.3
44	− 54.598	− 67.619	2011	2013	14	D	G	SCO	13.4 ± 0.4	6.7 ± 0.3
45	− 54.741	− 67.829	1993	2011	54	T/A	G	SCO	13.2 ± 0.3	8.2 ± 0.2
46	− 54.680	− 67.340	2000	2014	667	D	G + R	SCO	13.6 ± 0.3	6.9 ± 0.2
47	− 54.593	− 68.268	2003	2014	126	D	G + R	SCO	13.7 ± 0.3	6.8 ± 0.2
48	− 54.882	− 67.625	2010	2013	15	D	G + R	SCO	14.1 ± 0.5	8.2 ± 0.4

[a] Before 2003 some sessions were shorter than 24 h. Nevertheless, they were also included in the GNSS analysis.
[b] D means "direct mount", T means "tripod", A means "adapter for direct mount".
[c] G means "GPS-only", G + R means "GPS + GLONASS".
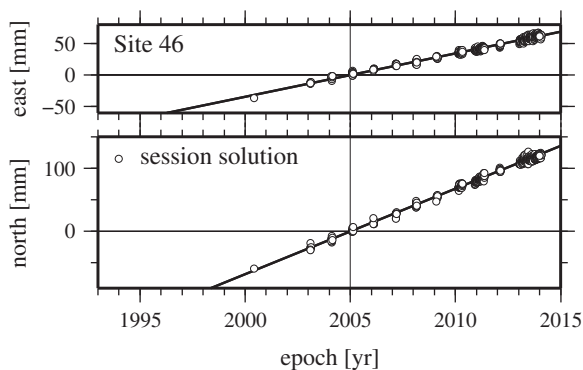[d] Continuously operated GNSS tracking station.

Fig. 3. Example of daily GNSS session solutions and the obtained horizontal linear trend (black solid lines, position reference epoch $t_0 = 2005.0$): regional site 46, located on the SCO plate, roughly 10 km south of the Fagnano Lake (see Table 1 and Fig. 2a).

from Thomas et al. (2003) into its global plate circuits closure. In contrast, the geologically constrained model NNR-MORVEL56 (Argus et al., 2011) predicts a larger rate of about 9 mm yr^{-1} for the same tectonic boundary. Our estimation agrees with the slip rate reported by Smalley et al. (2003) (6.6 ± 1.3 mm yr^{-1}), who also suggested that not all SCO-SAM relative motion in the area is accommodated by MFS. However, our observations are restricted to the TDF main island and their distribution is not broad enough to be conclusive about this interpretation. On the other hand, the residual deformation shows no indication of aseismic creeping on any of the modeled fault segments (Fig. 5).

Our model results in a locking depth of 11^{+5}_{-5} km, a value comparable to results for other strike-slip plate boundaries (e.g. Thatcher, 1990; Murray and Segall, 2001). This fairly shallow locking depth is consistent with a Moho depth of 26 ± 5 km, as predicted by the model GEMMA2012C, which combines CRUST2.0 (Bassin et al., 2000) with gravity data from GOCE (Reguzzoni et al., 2013). Hence, it is reasonable to expect a small D/H ratio between locking depth
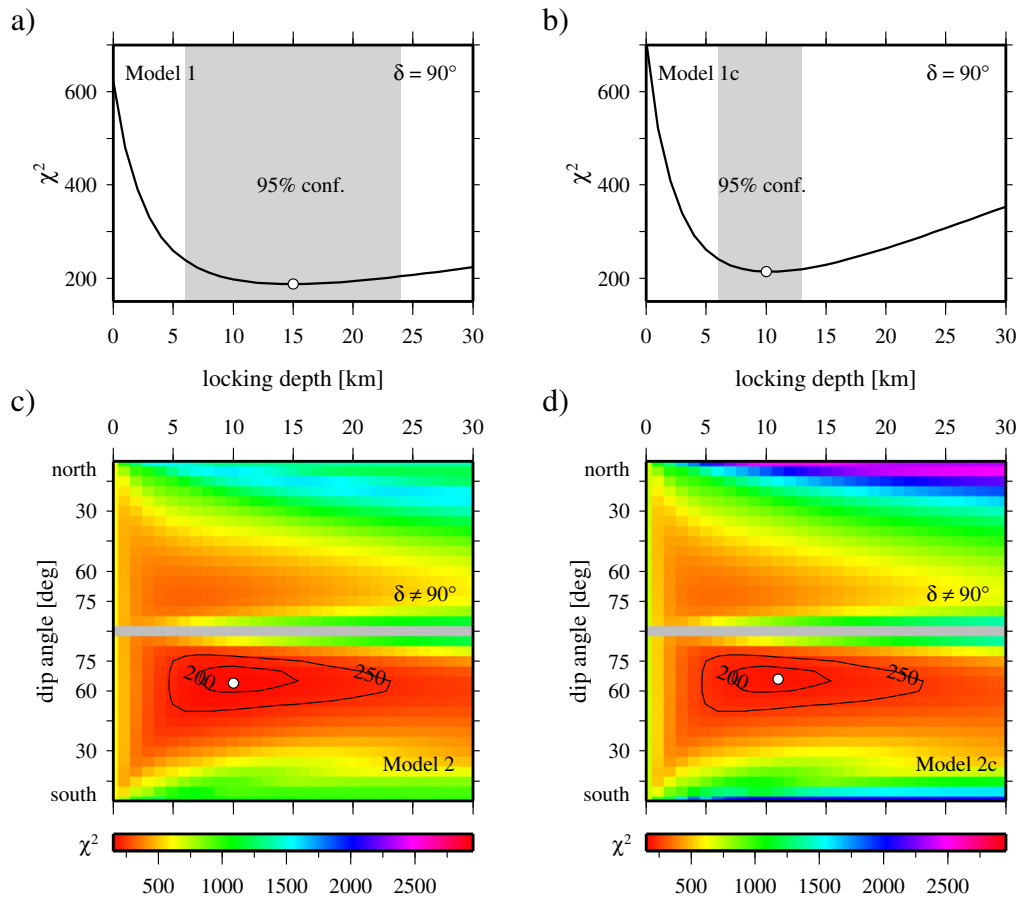
Fig. 4. Results of the optimum-fit search for the non-linear parameters dip angle (δ) and locking depth (D): a) models with vertical dislocations and inversion of geodetic observations only; b) same as a) but additional geophysical constraints applied; c) models with inclined dislocations and inversion of geodetic observations only; d) same as c) but additional geophysical constraints applied (preferred model). In each case, the white circle indicates the optimum solution.

(D) and lithosphere thickness (H) for our elastic model. On the other hand, faults dipping $66^{+6}_{-4}°$ southward, as predicted from our model, agree with the inclination of ~ 75° reported (graphically) by Tassone et al. (2005) from interpretation of gravimetric data and structural observations. Within its formal uncertainty, our findings also agree with the inclination of 90° ± 40° given by Smalley et al. (2003), from inversion of an independent set of geodetic observations. According to our back-slip model this inclination corresponds to the upper (and locked) end of the modeled fault segments. However, our data do not have enough spatial resolution to reliably resolve

the upward-branching arrangement of faults, generally associated to strike-slip fault zones, and reported by Esteban et al. (2014) for the MFS from the interpretation of active seismic survey profiles. Due to the same reason, our model could not resolve the slip partitioning between the several strands that accommodate the movement near the surface (see Fig. 2a). It should be expected that the estimated rates may be greater than the rates on individual strands, where multiple strands accommodate the strain.

In addition, our model predicts segments with opening movement (i.e., normal faulting) along central eastern MFS, also reported by several

Table 2
Estimated Euler poles and rotation rates.

	Block (modeling)	Latitude deg	Longitude deg	Rate deg Myr^{-1}	1 − σ error ellipse[a]			Error in rate	$\chi2$
					Semi-maj.	Semi-min.	Azi.		
Model 1	SAM	50.9	152.8	+0.304	6.8	2.3	111	0.076	187.2
	SCO	52.2	−165.6	+0.206	26.0	14.1	126	0.101	
	SCO (fixed SAM)	−29.7	−67.8	+0.147	27.2	1.8	180	0.153	
Model 1c	SAM	−12.7	−134.6	+0.141	1.5	0.2	172	0.002	213.8
	SCO	−7.3	−116.2	+0.165	6.6	0.3	177	0.012	
	SCO (fixed SAM)	10.0	−64.2	+0.056	23.8	0.4	0	0.011	
Model 2	SAM	−25.6	−123.1	+0.171	15.3	8.1	145	0.048	167.6
	SCO	57.3	−179.3	+0.247	11.7	4.9	116	0.074	
	SCO (fixed SAM)	64.2	111.0	+0.314	3.8	2.2	150	0.116	
Model 2c (preferred model)	SAM	−12.5	−134.0	+0.142	1.4	0.2	172	0.002	185.9
	SCO	−2.1	−117.5	+0.161	6.5	0.0	180	0.009	
	SCO (fixed SAM)	27.0	−63.4	+0.055	24.4	2.1	3	0.004	
Drewes (2009)	SCO plate	−14.6	−122.0	+0.123	1.4	0.9	90	0.002	
Thomas et al. (2003)	SCO plate (fixed SAM)	19.1	−56.9	+0.067	40.3	2.9	177	0.010	

[a] Axis in geocentric degrees; azimuth of semi-major axis in degrees clockwise from due north.

Table 3
Estimated slip rates and optimum dip angles and locking depths.

	Fault segment (modeling)	Strike-slip rate[a] mm yr^{-1}	Dip-slip rate[a] mm yr^{-1}	Fault-perp. rate[b] mm yr^{-1}	Tensile-slip rate[a] mm yr^{-1}	Dip angle[c] deg	Locking depth[c] km
Model 1	1	+6.8±0.3			−0.6±0.5	90	15^{+9}_{-7}
	2	+6.8±0.3			+0.3±0.4	90	15^{+9}_{-7}
	3	+6.5±0.2			−2.0±0.4	90	15^{+9}_{-7}
Model 1c	1	+5.6±0.2			+0.1±0.3	90	10^{+3}_{-4}
	2	+5.5±0.2			+0.7±0.3	90	10^{+3}_{-4}
	3	+5.4±0.2			−1.4±0.3	90	10^{+3}_{-4}
Model 2	1	+6.0±0.2	−1.8±0.6	+0.7±0.3		64^{+6}_{-6}	10^{+5}_{-4}
	2	+5.9±0.2	−1.4±0.4	+0.6±0.2		64^{+6}_{-6}	10^{+5}_{-4}
	3	+5.6±0.2	+4.8±0.6	−2.1±0.3		64^{+6}_{-6}	10^{+5}_{-4}
Model 2c (preferred model)	1	+6.0±0.2	−0.3±0.4	+0.1±0.2		66^{+6}_{-4}	11^{+5}_{-5}
	2	+5.9±0.2	−1.8±0.4	+0.7±0.2		66^{+6}_{-4}	11^{+5}_{-5}
	3	+5.8±0.2	+3.8±0.4	−1.5±0.2		66^{+6}_{-4}	11^{+5}_{-5}

[a] Same conventions as in Okada (1985): positive strike-slip rates give left-lateral motion; positive and negative dip-slip rates indicate that the southern block goes up and down, respectively; positive and negative tensile-slip rates give opening and closing motion, respectively. Slip rates have been computed at the segment midpoint.

[b] Fault-perpendicular component of the estimated dip-slip rate; positive and negative fault-perpendicular rates give opening and closing motion, respectively.

[c] Optimum value with 95% confidence interval.

geological studies (e.g., Tassone et al., 2005; Ghiglione and Ramos, 2005; Menichetti et al., 2008). These new results also agree with our earlier identification of surface stretching along the MFS (Mendoza et al., 2011), based on geodetic observations that were also included in the present analysis. In our elastic model, the tensile component of deformation should be interpreted as an approximate representation of the compressional and extensional structures adjacent to predominantly strike-slip boundaries. In this particular case, a releasing bend provides for transtension (Lodolo et al., 2003), commonly accompanied by surface extension and subsidence (Sylvester, 1988). Therefore, our findings seem to be consistent with the structural interpretation of central eastern Fagnano Lake as composed by pull-apart basins (Esteban et al., 2014).

Applying a purely elastic model in our analysis, we implicitly assumed a small D/H ratio between locking depth and lithosphere thickness. Savage and Prescott (1978) have shown that, in this case, the effect of asthenosphere relaxation will not be important and a half-space elastic model should adequately approximate the deformation of a viscoelastic Earth. The excellent fit of our preferred model with the observations, and the shallow locking depth required to do so, seem to validate our hypothesis.
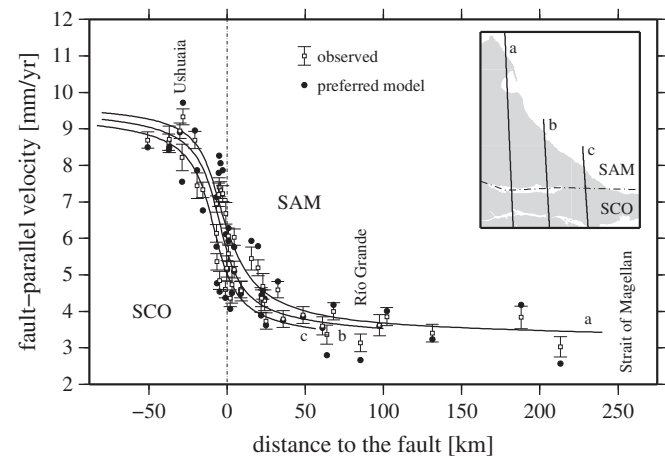

Fig. 5. Observed and predicted fault-parallel velocities (with respect to the IGS08 frame) are plotted as a function of the distance to the fault. Predicted profiles corresponding to three tracks are also shown (tracks a, b and c, see inset). The plot clearly shows the signal of ~ 6 millimeters per year of left lateral movement accommodated across the fault.

References

Argus, D.F., Gordon, R.G., DeMets, C., 2011. Geologically current motion of 56 plates relative to the no-net-rotation reference frame. Geochem. Geophys. Geosyst. 12. http://dx.doi.org/10.1029/2011GC003751.

Árnadóttir, T., Segall, P., 1994. The 1989 Loma Prieta earthquake imaged from inversion of geodetic data. J. Geophys. Res. Solid Earth 99, 21835–21855. http://dx.doi.org/10.1029/94JB01256.

Bassin, C., Laske, G., Masters, G., 2000. The current limits of resolution for surface wave tomography in North America. EOS, Trans. Am. Geophys. Un, p. F897.

Battaglia, M., Cervelli, P.F., Murray, J.R., 2013a. dMODELS: a MATLAB software package for modeling crustal deformation near active faults and volcanic centers. J. Volcanol. Geotherm. Res. 254, 1–4. http://dx.doi.org/10.1016/j.jvolgeores.2012.12.018.

Battaglia, M., Cervelli, P.F., Murray, J.R., 2013b. Volcanic monitoring. Modeling Crustal Deformation near Active Faults and Volcanic Centers — A Catalog of Deformation Models volume B1. U.S. Department of the Interior and U.S. Geological Survey, p. 96 (Chapter, URL: http://pubs.usgs.gov/tm/13/b1).

Bird, P., 2003. An updated digital model of plate boundaries. Geochem. Geophys. Geosyst. 4. http://dx.doi.org/10.1029/2001GC000252.

Boehm, J., Niell, A., Tregoning, P., Schuh, H., 2006. Global Mapping Function (GMF): a new empirical mapping function based on numerical weather model data. Geophys. Res. Lett. 33. http://dx.doi.org/10.1029/2005GL025546.

Dach, R., Hugentobler, U., Fridez, P., Meindl, M. (Eds.), 2007. Bernese GPS Software 5.0. Astronomical Institute, University of Bern, Bern, Switzerland.

Del Cogliano, D., Perdomo, R., Hormaechea, J.L., Olivero, E., Strelin, J., Martinioni, D., 2000. GPS detection of movements between SCO and SAM plates in the Argentinean part of Tierra del Fuego Island. 31st International Geological Congress, Rio de Janeiro, Brasil (6–17 August 2000).

Drewes, H., 2009. The actual plate kinematic and crustal deformation model APKIM2005 as basis for a non-rotating ITRF. In: Drewes, H. (Ed.), Geodetic Reference Frames. International Association of Geodesy Symposia volume 134. Springer, Berlin Heidelberg, pp. 95–99. http://dx.doi.org/10.1007/978-3-642-00860-3_15.

Esteban, F.D., Tassone, A., Lodolo, E., Menichetti, M., Lippai, H., Waldmann, N., Darbo, A., Baradello, L., Vilas, J.F., 2014. Basement geometry and sediment thickness of Lago Fagnano (Tierra del Fuego). Andean Geol. 41, 293–313. http://dx.doi.org/10.5027/andgeoV41n2-a02.

Freymueller, J.T., Murray, M.H., Segall, P., Castillo, D., 1999. Kinematics of the Pacific-North America Plate Boundary Zone, northern California. J. Geophys. Res. Solid Earth 104, 7419–7441. http://dx.doi.org/10.1029/1998JB900118.

Fritsche, M., Dietrich, R., Knöfel, C., Rülke, A., Vey, S., Rothacher, M., Steigenberger, P., 2005. Impact of higher-order ionospheric terms on GPS estimates. Geophys. Res. Lett. 32. http://dx.doi.org/10.1029/2005GL024342.

Fritsche, M., Soś'nica, K., Rodrguez-Solano, C.J., Steigenberger, P., Wang, K., Dietrich, R., Dach, R., Hugentobler, U., Rothacher, M., 2014. Homogeneous reprocessing of GPS, GLONASS and SLR observations. J. Geod. 1–18. http://dx.doi.org/10.1007/s00190-014-0710-3.

Ghiglione, M.C., Ramos, V.A., 2005. Progression of deformation and sedimentation in the southernmost Andes. Tectonophysics 405, 25–46.

Kreemer, C., Holt, W.E., Haines, A.J., 2003. An integrated global model of present-day plate motions and plate boundary deformation. Geophys. J. Int. 154, 8–34. http://dx.doi.org/10.1046/j.1365-246X.2003.01917.x.

Kreemer, C., Lavallée, D.A., Blewitt, G., Holt, W.E., 2006. On the stability of a geodetic no-net-rotation frame and its implication for the International Terrestrial Reference Frame. Geophys. Res. Lett. 33. http://dx.doi.org/10.1029/2006GL027058.

Kreemer, C., Blewitt, G., Klein, E.C., 2014. A geodetic plate motion and Global Strain Rate Model. Geochem. Geophys. Geosyst. 15, 3849–3889. http://dx.doi.org/10.1002/2014GC005407.

Lodolo, E., Menichetti, M., Bartole, R., Ben-Avraham, Z., Tassone, A., Lippai, H., 2003. Magallanes-Fagnano continental transform fault (Tierra del Fuego, southernmost South America). Tectonics 22. http://dx.doi.org/10.1029/2003TC001500.

Mao, A., Harrison, C.G.A., Dixon, T.H., 1999. Noise in GPS coordinate time series. J. Geophys. Res. Solid Earth 104, 2797–2816. http://dx.doi.org/10.1029/1998JB900033.

Meade, B.J., Hager, B.H., 2005. Block models of crustal motion in Southern California constrained by GPS measurements. J. Geophys. Res. Solid Earth 110. http://dx.doi.org/10.1029/345 2004JB003209.

Mendoza, L., Perdomo, R., Hormaechea, J.L., Del Cogliano, D., Fritsche, M., Richter, A., Dietrich, R., 2011. Present-day crustal deformation along the Magallanes-Fagnano Fault System in Tierra del Fuego from repeated GPS observations. Geophys. J. Int. 184, 1009–1022. http://dx.doi.org/10.1111/j.1365-246X.2010.04912.x.

Menichetti, M., Lodolo, E., Tassone, A., 2008. Structural geology of the Fuegian Andes and Magallanes fold-and-thrust belt — Tierra del Fuego Island. Geol. Acta 6, 19–42.

Moody, J.D., Hill, M.J., 1956. Wrench-fault tectonics. Geol. Soc. Am. Bull. 67, 1207–1246. http://dx.doi.org/10.1130/0016-7606(1956)67[1207:WT]2.0.CO;2.

Murray, M.H., Segall, P., 2001. Modeling broadscale deformation in northern California and Nevada from plate motions and elastic strain accumulation. Geophys. Res. Lett. 28, 4315–4318. http://dx.doi.org/10.1029/2001GL013373.

Okada, Y., 1985. Surface deformation due to shear and tensile faults in a half-space. Bull. Seismol. Soc. Am. 75, 1135–1154.

Pelayo, A.M., Wiens, D.A., 1989. Seismotectonics and relative plate motions in the Scotia Sea region. J. Geophys. Res. Solid Earth 94, 7293–7320. http://dx.doi.org/10.1029/JB094iB06p07293.

Petit, G., Luzum, B., 2010. IERS Conventions (2010). Technical Report 36. IERS Conventions Centre.

Rebischung, P., Griffiths, J., Ray, J., Schmid, R., Collilieux, X., Garayt, B., 2012. IGS08: the IGS realization of ITRF2008. GPS Solutions 16, 483–494. http://dx.doi.org/10.1007/s10291-011-0248-2.

Reguzzoni, M., Sampietro, D., Sansò, F., 2013. Global Moho from the combination of the CRUST2.0 model and GOCE data. Geophys. J. Int. 195, 222–237. http://dx.doi.org/10.3701093/gji/ggt247.

Rodrguez, E., Morris, C.S., Belz, J.E., Chapin, E.C., Martin, J.M., Daffer, W., Hensley, S., 2005. An assessment of the SRTM topographic products. Technical Report JPL D-31639. Jet Propulsion Laboratory, Pasadena, USA (http://www2.jpl.nasa.gov/srtm/SRTM_D31639.pdf).

Savage, J.C., Prescott, W.H., 1978. Asthenosphere readjustment and the earthquake cycle. J. Geophys. Res. Solid Earth 83, 3369–3376. http://dx.doi.org/10.1029/JB083iB07p03369.

Savcenko, R., Bosch, W., 2012. EOT11a — empirical ocean tide model from multi-mission satellite altimetry. Technical Report DGFI 89. Deutsches Geodätisches Forschungsinstitut, Alfons-Goppel-Str. 11, D-80539 München, Germany.

Shen, Z.-K., Jackson, D.D., Kagan, Y.Y., 2007. Implications of geodetic strain rate for future earthquakes, with five-year forecast of M5 earthquakes in Southern California. Seismol. Res. Lett. 78, 116–120.

Smalley, R., Kendrick, E., Bevis, M.G., Dalziel, I.W.D., Taylor, F., Laura, E., Barriga, R., Casassa, G., Olivero, E., Piana, E., 2003. Geodetic determination of relative plate motion and crustal deformation across the Scotia-South America plate boundary in eastern Tierra del Fuego. Geochem. Geophys. Geosyst. 4. http://dx.doi.org/10.1029/2002GC000446.

Sylvester, A.G., 1988. Strike-slip faults. Geol. Soc. Am. Bull. 100, 1666–1703. http://dx.doi.org/10.1130/0016-7606(1988)100<1666:SSF>2.3.CO;2.

Tassone, A., Lippai, H., Lodolo, E., Menichetti, M., Comba, A., Hormaechea, J.L., Vilas, J.F., 2005. A geological and geophysical crustal section across the Magallanes-Fagnano fault in Tierra del Fuego. J. S. Am. Earth Sci. 19, 99–109.

Thatcher, W., 1990. Present-day crustal movements and the mechanics of cyclic deformation. The San Andreas Fault System, California, Number 1515 in U.S. Geol. Soc. Prof. Pap, pp. 189–205.

Thomas, C., Livermore, R., Pollitz, F., 2003. Motion of the Scotia sea plate. Geophys. J. Int. 115, 789–804.

Williams, S.D.P., 2003. The effect of coloured noise on the uncertainties of rates estimated from geodetic time series. J. Geod. 76, 483–494. http://dx.doi.org/10.1007/400s00190-002-0283-4.